RSC Advances

PAPER

View Article Online
View Journal | View Issue

Cite this: *RSC Adv.*, 2025, **15**, 23559

Multifunctional separator engineering *via* $FeCo_2O_4$ nanosheets and conductive additives for high-rate Li–S batteries†

Nannan Meng, Yicong Li, Ziming Tong, Zhaogen Wang * and Yuping Wu*

The growing demand for energy storage has driven significant research interest in lithium–sulfur (Li–S) batteries. However, the commercialization of Li–S batteries has been hindered by several challenges, among which the polysulfide shuttle effect is especially prominent. In this study, we synthesized binary transition-metal oxide $FeCo_2O_4$ nanosheets (FCO) *via* a hydrothermal precipitation reaction followed by high-temperature calcination. By simply coating FCO and Super P (SP) onto a polypropylene separator, we developed a modified separator (FCOSP) to enhance the battery performances. The FCO surface is abundant in catalytic and adsorptive active sites, effectively mitigating the polysulfide shuttle effect and thereby improving the battery performances. Meanwhile, SP not only enhances the conductivity of the coating but also contributes to the adsorption of polysulfides. The Li–S batteries assembled with FCOSP exhibit a decay rate of 0.083% after 1000 cycles at 1C. More remarkably, the capacity decay rate is as low as 0.07% after 1000 cycles at 5C. The effectiveness of $FeCo_2O_4$ in adsorbing and catalytically converting polysulfides is demonstrated, thus providing a viable approach for the commercialization of Li–S batteries.

Received 1st May 2025
Accepted 4th June 2025

DOI: 10.1039/d5ra03082j

rsc.li/rsc-advances

1 Introduction

The burgeoning electric vehicle industry has spurred an ongoing quest for superior energy storage systems.[1–4] Lithium–sulfur (Li–S) batteries have emerged as a promising candidate among various secondary batteries, distinguished by their high theoretical capacity (1675 mAh g^{-1}) and energy density (2600 Wh kg^{-1}).[5–7] Moreover, sulfur has attracted extensive attention due to its naturally abundant reserves, low cost, and environmental friendliness.[8,9] However, before achieving commercialization, Li–S batteries are confronted with numerous obstacles, among which the polysulfide shuttle effect and significant corrosion caused by side reactions of the lithium anode are particularly pronounced, impeding the application and development of Li–S batteries.[7,10,11]

To address the aforementioned issues, researchers have proposed numerous solutions targeting the battery structure. To enhance the chemical reaction kinetics and restrict sulfur mobility, various composites of carbon materials and inorganic compounds have been introduced into the cathode, thereby improving the electrochemical performance of Li–S batteries.[12,13] On the anode side, the deliberate design of specialized protective layers has been proven to effectively enhance the stability of Li–S batteries. These protective layers, which can be composed of inorganic materials, organic polymers, or inorganic–organic hybrid layers, serve to strengthen the lithium–electrolyte interface and mitigate issues such as dendrite formation and corrosion.[7,14,15] These solutions can significantly enhance battery performance. However, the structural design and fabrication of functional materials often require substantial time and cost, which are not conducive to the promotion and application of Li–S batteries.

As a crucial component of batteries, the separator has garnered extensive research attention. A substantial body of literature indicates that, compared to optimization strategies for the cathode and anode, simple modifications to the separator can significantly enhance the electrochemical performance of batteries.[7,16] The separator in a battery primarily serves to isolate the cathode and provide a pathway for the transportation of lithium ions.[17,18] Separator modification, a method of adding a functional layer to the separator, is typically achieved through a simple coating process. The addition of the functional layer often serves to facilitate electrochemical reactions and adsorb polysulfides, while also enhancing ionic conductivity and providing a platform for the uniform deposition of lithium ions.[7,18] Therefore, numerous researchers have explored modified separators, achieving many remarkable accomplishments that have advanced the development of Li–S batteries by addressing challenges from the separator aspect.

Herein, we successfully synthesized $FeCo_2O_4$ nanosheets *via* a co-precipitation method followed by calcination, and

Nanjing Tech University, Jiangsu Province, China. E-mail: wangzhaogen@njtech.edu.cn

† Electronic supplementary information (ESI) available. See DOI: https://doi.org/10.1039/d5ra03082j

subsequently coated $FeCo_2O_4$/Super P onto one side of the separator using a simple scraping method, resulting in the fabrication of the FCOSP-modified separator. Numerous empirical investigations have conclusively demonstrated that metal oxides exhibit remarkable catalytic potency toward polysulfide species. A defining characteristic of such materials is the presence of O^{2-} ions, which imbue their surfaces with pronounced polarity.[19] This attribute renders them particularly suitable as composite membrane materials in Li–S battery architectures.[20–34] Among the widely used metal oxides are TiO_2,[35] MnO_2,[36] Fe_3O_4 (ref. 37) and Co_3O_4.[38] In this research, we employed a binary transition metal oxide, $FeCo_2O_4$, which possesses abundant adsorption and catalytic active sites on its surface.[39–41] Fundamentally addressing the shuttle effect of polysulfides while simultaneously facilitating the forward progress of electrochemical reactions.[42–46] Super P, a typical conductive carbon nanoparticle, has been found to enhance the utilization of active cathode materials when used as a coating layer on separators. It can mitigate the shuttle effect of polysulfides to some extent, provide reaction sites for polysulfides, and reduce charge transfer resistance.[47,48] In our research, we found that combining the two as a functional layer for the separator of a Li–S battery can significantly mitigate the impact of the shuttle effect, resulting in significantly enhanced cycling stability and capacity of the battery.

2 Experimental

2.1 Synthesis of $FeCo_2O_4$ nanosheets

First, 0.202 g of $Fe(NO_3)_3 \cdot 9H_2O$ and 0.291 g of $Co(NO_3)_2 \cdot 6H_2O$ were homogeneously dispersed in 50 mL of deionized water and sonicated for 30 min. Subsequently, 0.3 g of urea ($CO(NH_2)_2$) was added to the resultant solution, which was then stirred for 1 h. The obtained suspension was transferred into a 100 mL stainless steel autoclave, heated to 120 °C at a ramping rate of 2 °C min^{-1} in a hydrothermal oven, and maintained at this temperature for 2 h. Following the reaction, the precipitate was isolated by centrifugation and washed repeatedly with deionized water. The as-synthesized Fe–Co precursor was dried in a vacuum oven at 60 °C for 12 h, after which it was transferred to a tube furnace and calcined at 400 °C for 2 h with a heating rate of 3 °C min^{-1}, yielding bulk $FeCo_2O_4$ solid. The calcined material was thoroughly ground into a fine powder for subsequent use.

2.2 Preparation of FCOSP separator

The modified separator was prepared using a traditional blade-coating method, as detailed below: First, $FeCo_2O_4$, Super P, and PVDF were mixed in a mass ratio of 1 : 8 : 1, and an appropriate amount of *N*-methylpyrrolidone (NMP) was added as a solvent. The mixture was thoroughly stirred to form a homogeneous slurry. Subsequently, the slurry was uniformly coated onto the surface of a commercial PP separator (Celgard 2400) using a blade. Following coating, the prepared separator was placed in a vacuum drying oven and dried at 60 °C for 6 hours to ensure complete curing of the slurry and strong adhesion to the separator. Finally, the dried separator was cut into circular pieces with a diameter of 19 mm for subsequent experiments, and the loading of FCOSP coating on each separator was 1.2–1.5 mg cm^{-2}.

2.3 Physical characterization

The crystalline structure of the as-synthesized samples was characterized by X-ray diffraction (XRD). Surface and morphological features were examined using scanning electron microscopy (SEM). Elemental composition and surface chemical states were determined *via* X-ray photoelectron spectroscopy (XPS). The specific surface area and pore size distribution were analyzed by Brunauer–Emmett–Teller (BET) measurements. The adsorption capacity of the samples toward Li_2S_6 solutions was evaluated using UV-visible absorption spectroscopy.

2.4 Electrochemical characterization

The cathode of the Li–S battery is a sulfur–carbon composite, and the anode is a lithium foil. The separator is PP, and the electrolyte is composed of 1 M LiTFSI with 1 wt% $LiNO_3$ in a DME/DOL (1 : 1, v/v) mixture. The S/CNTs cathode material was prepared by the melt-diffusion method. Sublimed sulfur and multi-walled carbon nanotubes (CNTs) were mixed and ground in a mass ratio of 7 : 3, sealed in a PTFE-lined autoclave under an argon atmosphere, and maintained at 155 °C for 12 h in a hydrothermal reactor. All battery assembly was conducted in an argon-filled glovebox with H_2O and O_2 levels below 1 ppm. The assembly sequence for the coin-type battery is as follows: cathode casing, cathode sheet, electrolyte, separator, electrolyte, anode sheet, spacer, spring, and anode casing. Cyclic voltammetry (CV) tests were performed on the CHI660e electrochemical workstation within a voltage range of 1.8–2.8 V. Electrochemical impedance spectroscopy (EIS) measurements were carried out on the CHI660e electrochemical workstation over a frequency range of 10^{-1} to 10^5 Hz with an amplitude of 5 mV. Galvanostatic charge–discharge tests were conducted using the LAND battery testing system. Symmetric Li_2S_6 batteries were assembled for CV testing with a voltage window of −1.0 to 1.0 V. Li_2S_8 batteries were assembled and tested on the CHI660e electrochemical workstation and LAND battery testing system for Li_2S nucleation experiments and GITT measurements.

3 Results and discussion

We successfully synthesized $FeCo_2O_4$ *via* a hydrothermal and co-precipitation method. To confirm the synthesis of $FeCo_2O_4$, X-ray diffraction (XRD) tests were conducted on the obtained material. As depicted in the XRD pattern (Fig. S1a, ESI†), the diffraction peaks of $FeCo_2O_4$ align with the standard card (JCPDS card no. 26-1136), clearly demonstrating the successful synthesis of $FeCo_2O_4$. Moreover, the absence of significant impurity peaks indicates a high purity of the synthesized material. To explore the elemental composition and valence distribution within the material, high-resolution X-ray

photoelectron spectroscopy (XPS) was conducted on the synthesized material. As shown in the broad spectrum (Fig. 1a), the $FeCo_2O_4$ material contains Fe, Co, C, and O elements. The presence of C is likely due to environmental contamination carbon. The Fe 2p spectrum (Fig. 1b) confirms the presence of Fe^{2+} and Fe^{3+} in the material,[49,50] while the Co 2p spectrum (Fig. 1c) indicates the existence of Co^{2+} and Co^{3+}.[49,51–53] The O 1s spectrum (Fig. 1d) is associated with the adsorption of hydroxyl groups (OH^-) in the defect and surface water environment.[54–57] $FeCo_2O_4$ nanosheets, leveraging mixed valence states of Fe and Co, feature a unique mixed-valence architecture that accelerates electron transfer. Meanwhile, the highly polar oxygen anions (O^{2-}) within the structure demonstrate robust polysulfide adsorption capability. Energy-dispersive spectroscopy (EDS) analysis (Fig. 1e–h) clearly reveals the uniform distribution of Fe, Co, and O elements, further confirming the successful synthesis of $FeCo_2O_4$ material. Scanning electron microscopy (SEM) observations (Fig. S2a–c, ESI†) reveal numerous grooves on the material surface, indicating a large specific surface area. This, in turn, provides more active sites for the adsorption and conversion of polysulfides. The N_2 adsorption/desorption isotherms of $FeCo_2O_4$ (Fig. S3a, ESI†) indicate a surface area of 95.957 $m^2\ g^{-1}$, with pore sizes mainly distributed around 10 nm (Fig. S3b, ESI†). The mesoporous structure is conducive to blocking polysulfides and enhancing battery stability. As depicted in the cross-sectional images of the modified coatings FCOSP and SP (Fig. S4a–f, ESI†), their respective thicknesses are 25 μm and 20 μm. Compared to the unmodified polypropylene (PP) separator, the denser coating effectively blocks polysulfides. Additionally, the incorporation of Super P enhances the transport rate of lithium ions. To illustrate the adsorption effect of different target samples on polysulfides, 15 mg of FCOSP, FCO, and SP were separately added to Li_2S_6 solution and left undisturbed for 12 h (Fig. 2a). The solution exhibited only slight changes when only SP was present, more significant changes when only FCO was present, and almost became colorless when FCOSP was used, indicating that FCOSP had the strongest adsorption capacity for polysulfides. Moreover, the decrease in Li_2S_6 absorption intensity was confirmed by UV-vis spectroscopy (Fig. 2b), with FCOSP showing the lowest absorption intensity, further demonstrating its superior adsorption effect on polysulfides.

To investigate the impact of different modified coatings on the redox kinetics, symmetric batteries with Li_2S_6 were assembled, where the electrodes of the symmetric battery were prepared by loading FCOSP and SP onto carbon paper. As shown in the cyclic voltammetry curves of the symmetric battery (Fig. 2c), no corresponding response current was observed in the symmetric battery without Li_2S_6 electrolyte, indicating that the response current is generated by the redox reaction of Li_2S_6. Additionally, the symmetric battery assembled with FCOSP electrodes exhibited larger redox currents and smaller polarization voltages compared to SP electrodes, suggesting that FCOSP can better facilitate the conversion between liquid polysulfides and solid Li_2S, a process that is also the main source of capacity in Li–S batteries. To further clarify the catalytic effect of FCOSP and SP electrodes on the phase transition of polysulfides

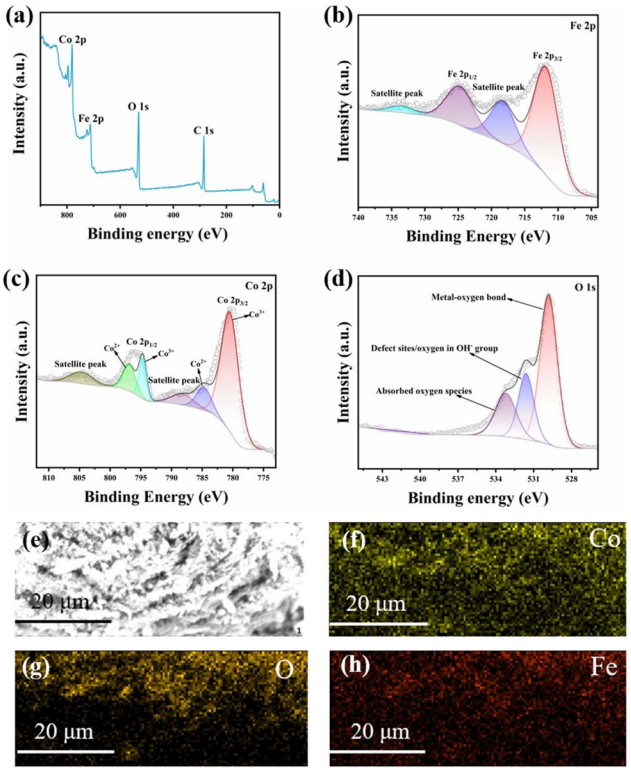

Fig. 1 Characterization of $FeCo_2O_4$. (a) XPS spectrum of $FeCo_2O_4$, (b) Fe 2p spectrum, (c) Co 2p spectrum, (d) O 1s spectrum, (e–h) EDS images of $FeCo_2O_4$ and corresponding elemental distributions of Co, O, and Fe.

from liquid to solid, additional studies were conducted. Through the Li_2S nucleation experiment (Fig. 2d and e), in accordance with Faraday's law,[58,59] the time required for the peak current of Li_2S nucleation on the FCOSP electrode was shorter (200 s). Simultaneously, the FCOSP electrode could achieve a higher peak current of 4.5 mA and a higher deposition capacity of 489.29 mAh g^{-1}, which is significantly higher than that of the SP electrode (2.3 mA and 238.69 mAh g^{-1}). This indicates that the addition of FCO significantly improved the kinetics of polysulfide conversion. GITT testing (Fig. 2f, g and S5a–d, ESI†) can further compare the polarization of FCOSP and SP electrodes during charge and discharge. Under constant current conditions, the internal resistance (ΔR) is proportional to ΔV, which corresponds to the voltage difference between the open-circuit voltage and the closed-circuit voltage point. The FCOSP electrode exhibited smaller internal resistance at the Li_2S nucleation and activation points, indicating high conductivity and enhanced Li_2S nucleation.

For research the impact of different modified coatings on the redox kinetics, symmetric Li//Li batteries with Li_2S_6 electrolyte were assembled, where the electrodes of the symmetric battery were prepared by loading FCOSP and SP onto carbon paper. Electrochemical impedance spectroscopy (EIS) was performed to determine the lithium-ion conductivity and Li^+ transference number in the liquid electrolyte. The EIS presented a straight line (Fig. 3a and S6a, ESI†), indicating that the carrier was solely

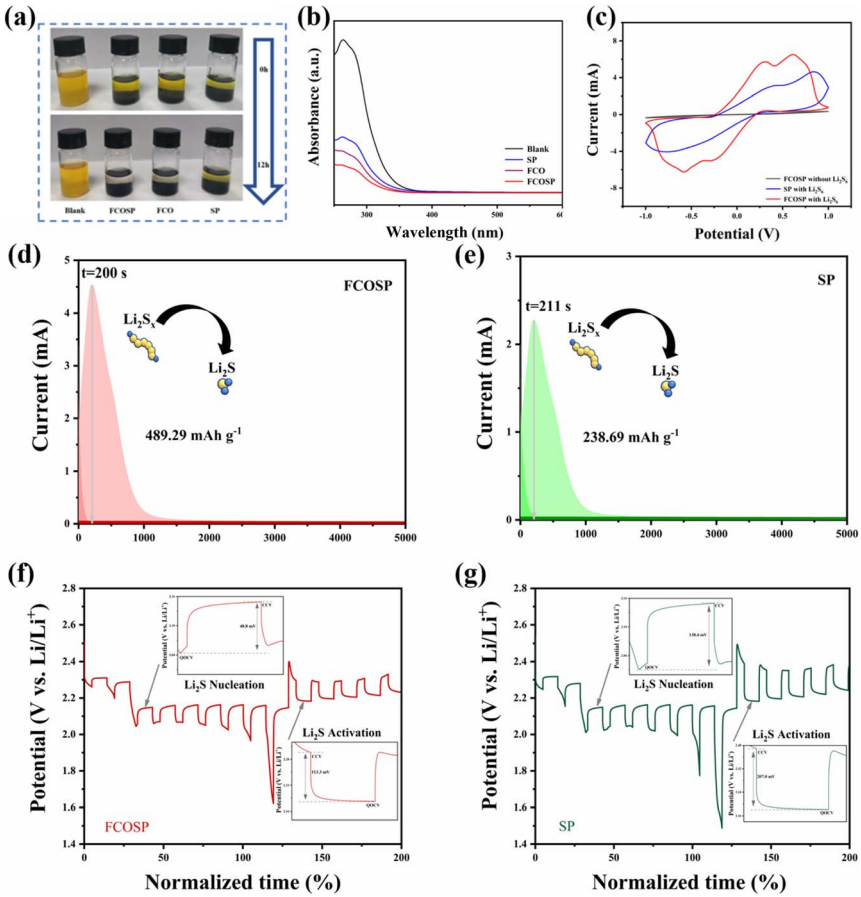

Fig. 2 Adsorption and electrochemical characterization of Li_2S_6. (a) Color changes of Li_2S_6 solution after adsorption by different adsorbents (blank, FCOSP, FCO, and SP), (b) UV-vis absorption spectra corresponding to different materials, (c) CV curves of Li_2S_6 symmetric cells at a scan rate of 3 mV s^{-1}, (d and e) chronoamperometric discharge curves of FCOSP and SP at 2.06 V, (f and g) GITT plots of Li_2S_8 batteries assembled with FCOSP and SP electrodes.

ionic.[60] The ionic conductivities of FCOSP, SP, and PP were 0.978, 0.749, and 0.702 mS cm^{-1}, respectively. The highest ionic conductivity of FCOSP at room temperature indicates that the addition of FCO enhances the chemical reaction kinetics. As shown in the contact angle test (Fig. S7, ESI†), the contact angles of FCOSP, SP, and PP were 12°, 23°, and 43°, respectively, 2 seconds after the addition of the electrolyte. This indicates that the addition of FCO enhances the affinity of the electrolyte,

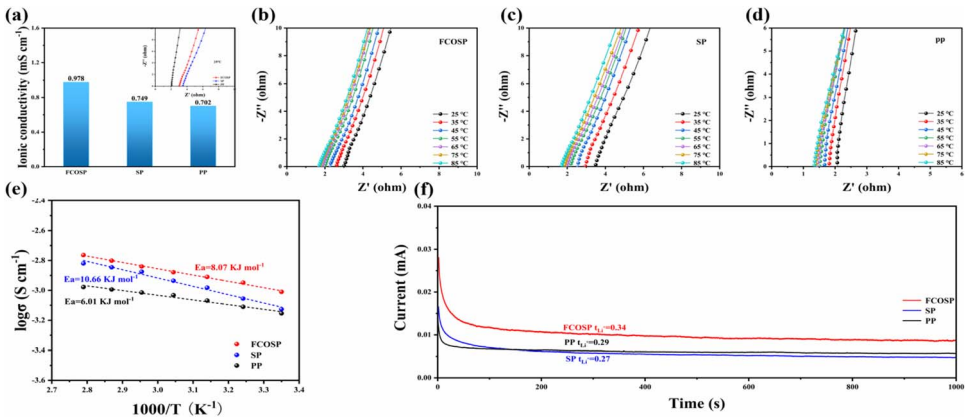

Fig. 3 Electrochemical characterization of different samples. (a) Ionic conductivity of different samples at 25 °C, (b–d) impedance spectra of symmetric cells with different samples at various temperatures, (e) Arrhenius plots corresponding to the impedance data of different samples, (f) *i–t* curves of Li//Li symmetric cells with different samples at 10 mV.

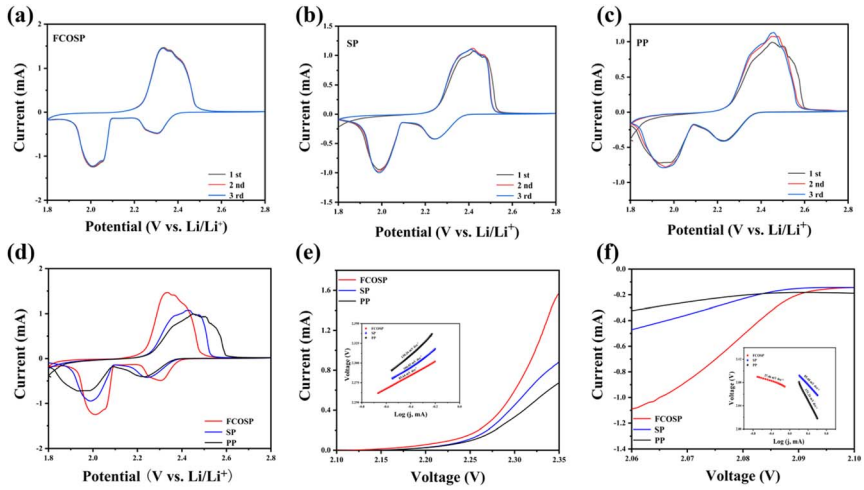

Fig. 4 Cyclic voltammetry (CV) and Tafel plots of different samples. (a) CV curves of the first three cycles for FCOSP at a scan rate of 0.1 mV s^{-1}, (b) CV curves of the first three cycles for SP at a scan rate of 0.1 mV s^{-1}, (c) CV curves of the first three cycles for PP at a scan rate of 0.1 mV s^{-1}, (d) first-cycle CV curves of different samples at a scan rate of 0.1 mV s^{-1}, (e and f) Tafel plots corresponding to the redox peaks of different samples.

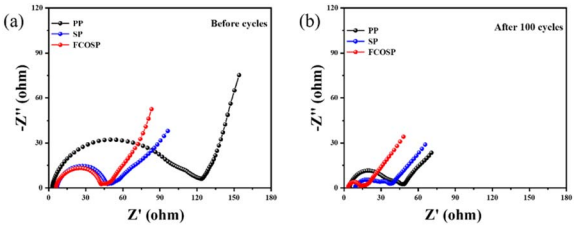

Fig. 5 Electrochemical impedance spectroscopy (EIS) of different samples. (a) Impedance spectra of different samples before 100 cycles, (b) impedance spectra of different samples after 100 cycles.

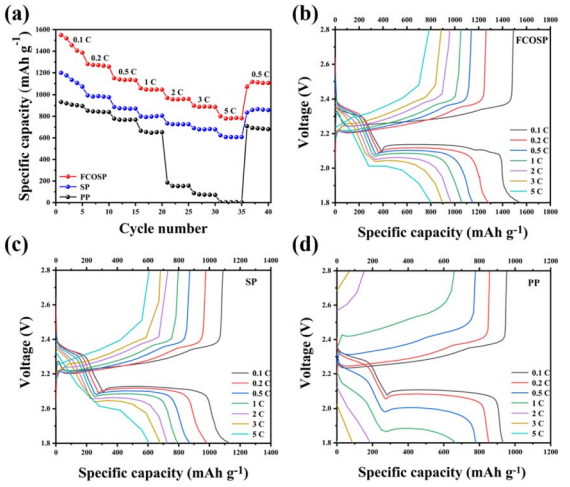

Fig. 6 Rate performance of Li–S batteries. (a) Rate performance tests of different samples, (b–d) corresponding charge–discharge curves for the rate performance tests of different samples.

and FCOSP exhibits the best compatibility with the electrolyte, consistent with the conclusion of the ionic conductivity at 25 °C. By testing the impedance of different separators at various temperatures (Fig. 3b–d) and fitting the Arrhenius plots (Fig. 3e), the activation energies of FCOSP, SP, and PP were found to be 8.07, 10.66, and 6.017 kJ mol^{-1}, respectively. The results show that the activation energy of FCOSP is lower than that of SP, indicating that FCO can reduce the energy barrier for charge transfer. The higher activation energies of both FCOSP and SP compared to PP may be due to the increased thickness of the separator caused by the coating. By assembling Li//Li symmetric batteries with different separators, the lithium-ion transference numbers of the three separators were determined. Based on the measured *i*–*t* curves and calculations from the Nyquist plots (Fig. 3f), the Li^+ transference numbers of FCOSP and SP were 0.34 and 0.27, respectively. Additionally, the Li^+ transference number of PP (0.29) was tested for comparison, which is consistent with previous research results.[61] After modification with SP, the Li^+ transference number showed a slight increase, while the enhancement was more pronounced after FCOSP modification, indicating that the addition of FCO is beneficial for Li^+ cation migration.

To study the impact of FCOSP on the electrochemical performance of Li–S batteries, Li–S batteries with FCOSP, SP, and PP separators were assembled (S/CNTs as the cathode and lithium foil as the anode). Cyclic voltammetry (CV) tests were conducted at a scan rate of 0.1 mV s^{-1} within the voltage range of 1.8–2.8 V. The CV curves of the three separators exhibited two reduction peaks at approximately 2.3 V and 2.0 V, representing the conversion of solid sulfur to soluble higher-order polysulfides and the subsequent reduction to insoluble sulfides (Li_2S_2/Li_2S), respectively. The anodic peaks were observed at around 2.4 V, corresponding to the reversible conversion of Li_2S_2/Li_2S to long-chain polysulfides and finally back to solid sulfur.[62] After cycling the different samples at the same scan rate for three cycles (Fig. 4a–c), the FCOSP curve showed the highest degree of overlap, indicating better battery reversibility and electrochemical stability, effectively mitigating the "shuttle effect". Comparing the first cycle CV (Fig. 4d) of the three types

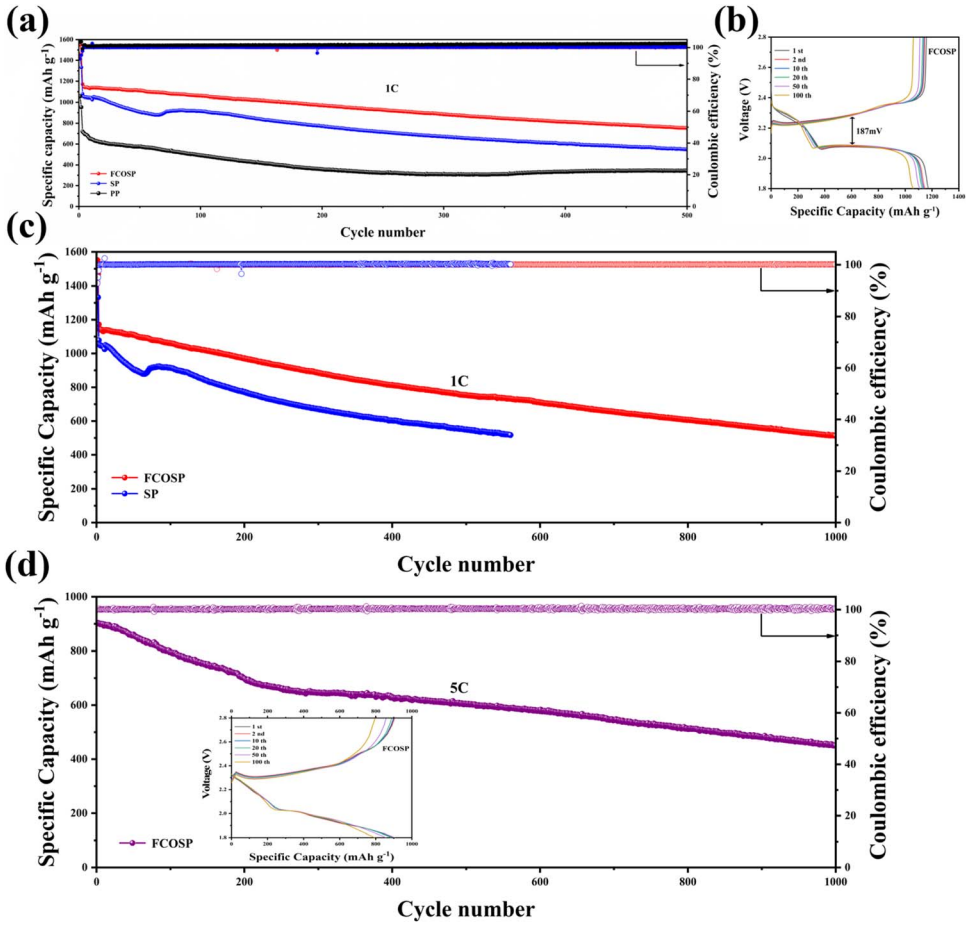

Fig. 7 Long-term cycling tests of Li–S batteries. (a) Cycling performance at 1C, (b) charge–discharge profiles of FCOSP at 1C, (c) comparison of long-term cycling between FCOSP and SP at 1C, (d) cycling performance of FCOSP at 5C.

of separators, it is further found that the FCOSP battery has the smallest gap between the reduction peak and the oxidation peak, indicating that FCOSP promotes the reduction of polarization in Li–S batteries. Additionally, the CV curve area of FCOSP was the largest, indicating that among the three separators, FCOSP provided the best enhancement to the battery's redox kinetics and improved sulfur utilization. The Tafel curves of the redox peaks (Fig. 4e, f and S8a, b, ESI†) showed that the Tafel slopes of the FCOSP battery (27.46 and 85.64 mV dec^{-1}) were lower than those of the SP battery (85.48 and 106.02 mV dec^{-1}) and the PP battery (151.26 and 130.26 mV dec^{-1}), indicating that FCOSP enhances the reaction kinetics of Li_2S reduction and oxidation.

To further investigate the sulfur redox kinetics of the three separators, CV tests were conducted at different scan rates ranging from 0.1 to 0.5 mV s^{-1}. The results, as shown in figure (Fig. S9a–c, ESI†), indicate a linear relationship between the peak current density and the square root of the scan rate for each current density. This suggests that the sulfur redox reaction is controlled by the ion diffusion process.[63] According to the Randles–Sevcik equation,[62] when comparing the batteries assembled with the three different separators, the FCOSP battery exhibited the highest slope and the largest ion diffusion coefficient (Fig. S9d–f and Table S1, ESI†). This indicates that FCO nanosheets the conversion of polysulfides, enhancing the utilization rate of sulfur.

After 100 cycles at 1C, EIS measurements were conducted on Li–S batteries with different separators before and after cycling to further investigate the reaction kinetics. The impedance curves of the three separators were fitted (Fig. S10 and Table S2, ESI†). To more intuitively show the impedance changes, the data were organized (Fig. 5a and b). The significant impedance changes before and after cycling are attributed to the dissolution and redistribution of sulfur during the redox reactions of the battery. Before cycling, the interfacial resistance (R_{SEI}) and charge transfer resistance (R_{CT}) of the FCOSP battery were 37.2 Ω and 34.6 Ω, respectively, lower than those of the SP (R_{SEI}: 40.7 Ω; R_{CT}: 45.8 Ω) and PP (R_{SEI}: 93.4 Ω; R_{CT}: 121.1 Ω) separators. After 100 cycles, the FCOSP-modified battery exhibited lower R_{CT} (9.9 Ω) and R_{SEI} (9.4 Ω) compared to SP (R_{SEI}: 24.1 Ω; R_{CT}: 19.5 Ω) and PP (R_{SEI}: 30.7 Ω; R_{CT}: 41.8 Ω). This indicates that both FCOSP and SP accelerated the charge transfer at the electrode surface, but the addition of FCO further enhanced the rate of charge transfer, reduced the energy barrier of sulfur redox reactions, and accelerated the reaction kinetics of Li–S batteries.

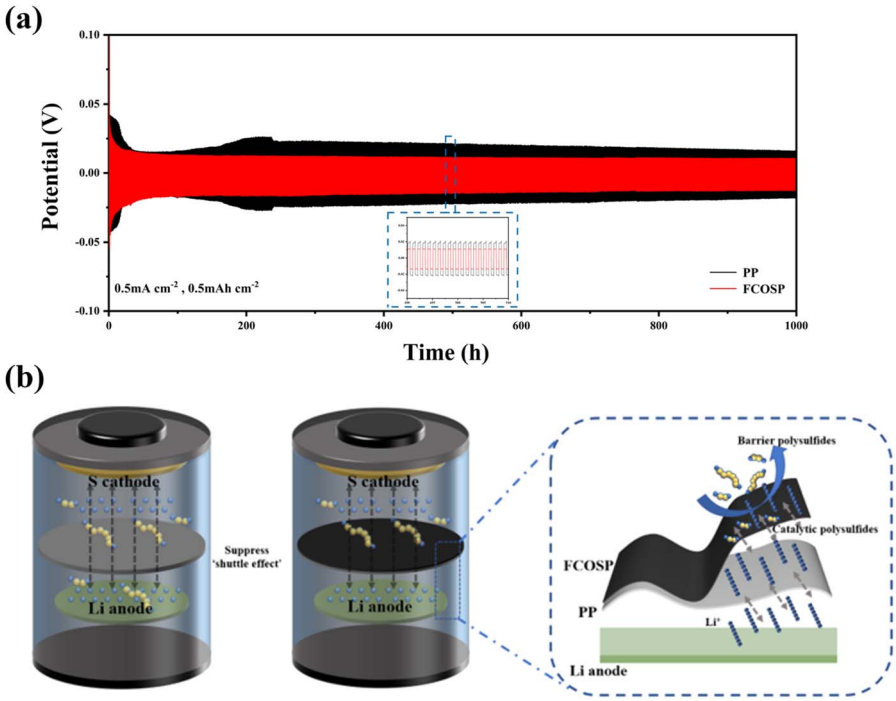

Fig. 8 (a) Voltage curves of Li//Li symmetrical cells with FCOSP and PP at 0.5 mA cm^{-2}, (b) schematic illustration of the role of FCOSP and commercial separator (PP) in Li–S batteries.

The electrochemical performance of Li–S batteries with different separators at various rates is shown in figure (Fig. 6a). The discharge specific capacities of the FCOSP battery at 0.1, 0.2, 0.5, 1, 2, 3, and 5C were 1550, 1281.7, 1151.2, 1059.3, 970.7, 898.3 and 801.2 mAh g^{-1}, respectively, demonstrating excellent rate performance, which is much higher than that of SP and PP batteries. As the current density increased, the capacity of all three batteries decreased significantly, but the capacity of the FCOSP battery remained superior to that of SP and PP batteries. The results indicate that compared with SP and PP batteries, the FCOSP battery is more kinetically favorable for sulfur conversion under different current densities. Additionally, the corresponding charge–discharge curves of the three batteries (Fig. 6b–d) clearly show that FCOSP has a longer and more stable redox reaction platform, which is better than that of SP batteries, while PP batteries cannot achieve the liquid–solid conversion involving Li_2S at high rates above 2C. These results demonstrate the feasibility of applying FCOSP in Li–S batteries.

The batteries with the three different separators were activated by cycling twice at 0.1C and then tested for cycle performance at 1C. As shown in figure (Fig. 7a), compared to the three batteries, the initial discharge capacity of the FCOSP battery was the highest at 1172.45 mAh g^{-1}. In addition, the capacity of the PP battery after 500 cycles was only 343.9 mAh g^{-1}, with a capacity decay rate of 0.148% per cycle. The SP battery had a capacity of 550.1 mAh g^{-1} after 500 cycles, with a capacity decay of 0.135% per cycle. In contrast, the FCOSP battery had a capacity of 753.9 mAh g^{-1} after 500 cycles at 1C, with a capacity decay rate as low as 0.089% per cycle. This indicates that FCOSP improved the utilization rate of the battery's cathode active material and effectively suppressed the "shuttle effect" in Li–S batteries. From the charge–discharge curves of the three batteries at 1C (Fig. 7b and S11, ESI†), it can be seen that the charge–discharge platforms of the FCOSP battery basically coincided during the cycling process, and its polarization voltage was lower than that of SP (255 mV) and PP (453 mV), at only 187 mV, demonstrating the superiority of FCOSP in Li–S batteries. To further prove the superiority of FCO in Li–S batteries, it can be seen from the figure (Fig. 7c and S12, ESI†) that the coulombic efficiency and capacity of the SP battery showed significant fluctuations after about 550 cycles at 1C, while the FCOSP battery did not exhibit this phenomenon even after 1000 cycles. The experimental results show that FCOSP has a good inhibitory effect on the "shuttle effect" in Li–S batteries, improving the electrochemical stability and cycle life of the battery.

The cycle performance test at high current density is a key indicator for the practical application of Li–S batteries. In this study, the FCOSP battery was tested at a current density of 5C (Fig. 7d and S13, ESI†). After initial activation, the discharge capacity of the FCOSP battery was 904 mAh g^{-1} in the first cycle. During 1000 cycles, the capacity decay rate per cycle was 0.07%, and the coulombic efficiency remained above 99% throughout the cycling process. Additionally, the charge–discharge curves at different cycle numbers basically coincided, indicating that FCOSP can maintain the stability of Li–S batteries at high current density. The results show that the Li–S battery with FCOSP has good cycle stability at high current density.

To visually demonstrate the blocking effect of the FCOSP separator on polysulfides, an H-shaped glass cell was assembled

(Fig. S14, ESI†). The left side of the glass cell contained Li_2S_6 solution, while the right side contained DME solvent. After being left undisturbed for 12 h, the right side of the glass cell with the FCOSP separator remained clear and transparent, while the right side of the glass cell with the SP separator was slightly yellow, and the right side of the glass cell with the PP separator was much darker. This result indicates that the FCOSP separator can effectively block the shuttle of polysulfides.

To further investigate the protective effect of FCOSP on the anode side of the battery, the separator and lithium sheet were disassembled after 100 cycles at a current density of 1C. As can be seen in the figure (Fig. S15, ESI†), the backside of the FCOSP separator exhibited the lightest yellow color, indicating that the FCOSP modified separator has good stability and the best blocking effect on polysulfides. Additionally, SEM images of the cycled lithium surface and cross-section (Fig. S16, ESI†) also showed that the lithium sheets in the FCOSP battery had less lithium dendrites and sulfur content than those in the SP and PP batteries, directly proving that the FCOSP coating can effectively block polysulfides and promote uniform lithium deposition. To further demonstrate the protective effect of FCOSP on the lithium anode, Li//Li symmetric batteries with FCOSP and PP were assembled for symmetric polarization tests (0.5 mA cm^{-2}, 0.5 mAh cm^{-2}). As shown in figure (Fig. 8a), after 1000 hours, the polarization voltage of the FCOSP symmetric battery was always lower than that of the PP battery, indicating that FCOSP allows for more uniform lithium deposition, thereby protecting the anode and enhancing the stability of the Li–S battery.

Assembling commercial separators and FCOSP-modified separators in Li–S batteries, the working schematic diagram is shown in figure (Fig. 8b). During battery operation, polysulfides diffuse from the cathode to the anode through the separator, leading to the loss of active material on the cathode side and volume expansion on the anode side, causing a series of safety issues. The designed FCOSP modified coating mainly consists of two parts. The first part is FCO, which has a large specific surface area and a large number of active sites, promoting the chemical reaction kinetics of Li–S batteries. The second part is SP, which provides good electrical conductivity and also restricts the shuttle of polysulfides to a certain extent. By combining the two in a certain proportion, the designed FCOSP modified separator can not only effectively block the "shuttle effect" of polysulfides but also has strong catalytic ability. While improving the redox kinetics of sulfur compounds, it can also induce the uniform nucleation of lithium sulfide, greatly increasing the utilization rate of sulfur.

4 Conclusions

In summary, this study successfully synthesized $FeCo_2O_4$ particles and fabricated a modified separator for Li–S batteries by simply coating FCO ($FeCo_2O_4$) and SP (Super P) in a certain proportion. Due to the presence of O^{2-} in $FeCo_2O_4$, metal oxides containing O^{2-} typically have a strong polarity on their surface. Additionally, the $FeCo_2O_4$ particles have numerous pores with diameters around 15 nm. The abundant porous structure provides a large specific surface area, enabling more adsorption and reaction sites. Super P can reduce the impedance in the charge transfer process, enhancing the kinetic reaction of S/S^{2-} coupling. The FCOSP-modified separator can increase sulfur utilization, enhance ionic conductivity, and facilitate uniform lithium-ion deposition, thereby improving the electrochemical stability and cycle life of Li–S batteries. In conclusion, the FCOSP battery achieved an initial discharge capacity of 1172.45 mAh g^{-1} at 1C, with a decay rate of 0.083% per cycle after 1000 cycles. At 5C, the initial discharge capacity reached 904 mAh g^{-1}, with a capacity decay rate as low as 0.07% per cycle after 1000 cycles. Compared to other reported separator modifications (Table S3, ESI†), this work clearly demonstrates high capacity and low decay rate while maintaining a longer cycle life and stability. Undoubtedly, this work paves a new way for the commercialization of functionalized separators in Li–S batteries.

Data availability

Data supporting the findings of this study are available from the corresponding author upon reasonable request. These data will not be publicly shared due to privacy constraints and ethical considerations.

Author contributions

Nannan Meng: conceptualization, methodology, visualization, investigation, formal analysis, data curation, writing – original draft, project administration, funding acquisition. Zhaogen Wang: writing – review, revision, supervision, project administration, funding acquisition.

Conflicts of interest

There are no conflicts to declare.

Acknowledgements

Financial support from the National Basic Research Program of China (2015CB655301), the National Natural Science Foundation of China (21706119), and the Program of Excellent Innovation Teams of Jiangsu Higher Education Institutions is gratefully acknowledged.

References

1 Z. Liang, J. Shen, X. Xu, F. Li, J. Liu, B. Yuan, Y. Yu and M. Zhu, *Adv. Mater.*, 2022, **34**, 2200102.
2 F. Wu, J. Maier and Y. Yu, *Chem. Soc. Rev.*, 2020, **49**, 1569–1614.
3 Y. Zhou, C. Yuan, S. Wang, Y. Zhu, S. Cheng, X. Yang, Y. Yang, J. Hu, J. He and Q. Li, *Energy Storage Mater.*, 2020, **28**, 255–263.
4 K. Kang, Y. S. Meng, J. Bréger, C. P. Grey and G. Ceder, *Science*, 2006, **311**, 977–980.

5 J. Castillo, L. Qiao, A. Santiago, X. Judez, A. S. de Buruaga, G. Jimenez, M. Armand, H. Zhang and C. J. E. M. Li, *Energy Mater.*, 2022, **2**, 200003.
6 T. Wang, J. He, Z. Zhu, X.-B. Cheng, J. Zhu, B. Lu and Y. Wu, *Adv. Mater.*, 2023, **35**, 2303520.
7 C.-X. Zhao, J.-N. Liu, B.-Q. Li, D. Ren, X. Chen, J. Yu and Q. Zhang, *Adv. Funct. Mater.*, 2020, **30**, 2003619.
8 R. Deng, F. Chu, F. Kwofie, Z. Guan, J. Chen and F. Wu, *Angew. Chem., Int. Ed.*, 2022, **61**, e202215866.
9 G. Zhao, K. Rui, S. X. Dou and W. Sun, *Adv. Funct. Mater.*, 2018, **28**, 1803291.
10 L. Pan, S. Sun, Y. Chen, P. Wang, J. Wang, X. Zhang, J.-J. Zou and Z. L. Wang, *Adv. Energy Mater.*, 2020, **10**, 2000214.
11 W. Zha, W. Li, Y. Ruan, J. Wang and Z. Wen, *Energy Storage Mater.*, 2021, **36**, 171–178.
12 H.-E. Wang, K. Yin, N. Qin, X. Zhao, F.-J. Xia, Z.-Y. Hu, G. Guo, G. Cao and W. Zhang, *J. Mater. Chem. A*, 2019, **7**, 10346–10353.
13 W. Zhu, W. Chai, M. Deng, D. Chen, D. Chen, J. Zhang, C. Zhang and Y. Hao, *Electrochim. Acta*, 2020, **330**, 135325.
14 Z. Wang, J. Liu, B. Zhang, L. Sun, L. Cong, L. Lu, A. Mauger, C. M. Julien, H. Xie and H. Sun, *Energy Storage Mater.*, 2020, **24**, 373–378.
15 P. Zheng, W. Zhou, Y. Mo, B. Zheng, M. Han, Q. Zhong, W. Yang, P. Gao, L. Yang and J. Liu, *J. Energy Chem.*, 2024, **100**, 730–738.
16 X. Liu, J. Meng, J. Zhu, M. Huang, B. Wen, R. Guo and L. Mai, *Adv. Mater.*, 2021, **33**, 2007344.
17 S. H. Chung and A. Manthiram, *Adv. Mater.*, 2014, **26**, 7352–7357.
18 P. Zeng, B. Su, X. Wang, X. Li, C. Yuan, G. Liu, K. Dai, J. Mao, D. Chao, Q. Wang and L. Zhang, *Adv. Funct. Mater.*, 2023, **33**, 2301743.
19 X. Liu, J.-Q. Huang, Q. Zhang and L. Mai, *Adv. Mater.*, 2017, **29**, 1601759.
20 Z. Li, Q. Zhang, L. Hencz, J. Liu, P. Kaghazchi, J. Han, L. Wang and S. Zhang, *Nano Energy*, 2021, **89**, 106331.
21 H. Pei, X. Guan, X. Chen, Y. Chen, Y. Yang, Y. Wen, H. Nie, L. Chang, X. Zhou, X. Xie, L. Ye and Y.-W. Mai, *Nano Energy*, 2024, **126**, 109680.
22 R. Qi, L. Zhao, P. Liu, Y. Zhen, X. Fu, X. Li, Y. Cui, T. Cai, Z. Yan, Q. Xue and W. Xing, *Energy Storage Mater.*, 2025, **75**, 104065.
23 W. Sun, X. Sun, Q. Peng, H. Wang, Y. Ge, N. Akhtar, Y. Huang and K. Wang, *Nanoscale Adv.*, 2019, **1**, 1589–1597.
24 R. Tao, S. Tan, X. Lyu, X.-G. Sun, J. Yang, D. Xie, Z. Du, K. Z. Pupek, S. Dai and J. Li, *Nano Energy*, 2024, **130**, 110091.
25 B. Wang, J. Tang, S. Jia, Z. Xing, S. Chen, Y. Deng, X. Meng and S. Tang, *Adv. Funct. Mater.*, 2024, **34**, 2315836.
26 S. Xia, Z. Chen, L. Yuan, J. Song, Q. Zhou, X. Yuan, L. Liu, L. Fu, Y. Chen and Y. Wu, *J. Mater. Chem. A*, 2023, **11**, 19870–19876.
27 S. Xia, J. Song, Q. Zhou, L. Liu, J. Ye, T. Wang, Y. Chen, Y. Liu, Y. Wu and T. van Ree, *Adv. Sci.*, 2023, **10**, 2301386.
28 J. Yan, F.-Q. Liu, J. Gao, W. Zhou, H. Huo, J.-J. Zhou and L. Li, *Adv. Funct. Mater.*, 2021, **31**, 2007255.
29 J. Zhou, C. Zhang, C. Xie, H. Wang, H. Fan, Y. Guo, C. Wang, F. Chen, Y. Ding, Q. Huang and Z. Zheng, *Adv. Energy Mater.*, 2024, **14**, 2303063.
30 T. Liu, X. Dong, B. Tang, R. Zhao, J. Xu, H. Li, S. Gao, Y. Fang, D. Chao and Z. Zhou, *J. Energy Chem.*, 2024, **98**, 311–326.
31 Y. Ma, L. Chang, D. Yi, M. Liu, P. Wang, S. Luo, Z. Zhang, Y. Yuan and H. Lu, *Energy Mater.*, 2024, **4**, 400059.
32 S. Xia, Z. Lin, B. Peng, X. Yuan, J. Du, X. Yuan, L. Liu, L. Fu, R. Holze and Y. Wu, *Energy Environ. Sci.*, 2024, **17**, 5461–5467.
33 J. Feng, C. Zhang, W. Liu, S. Yu, L. Wang, T. Wang, C. Shi, X. Zhao, S. Chen, S. Chou and J. Song, *Angew. Chem., Int. Ed.*, 2024, **63**, e202407042.
34 Z.-H. Luo, M. Zheng, M.-X. Zhou, X.-T. Sheng, X.-L. Chen, J.-J. Shao, T.-S. Wang and G. Zhou, *Adv. Mater.*, 2025, **37**, 2417321.
35 Z. Li, C. Zhou, J. Hua, X. Hong, C. Sun, H.-W. Li, X. Xu and L. Mai, *Adv. Mater.*, 2020, **32**, 1907444.
36 Z. Ma, Z. Qi, G. Song, S. Huang, Z. Du, J. Dong, C. Guan, P. Luo, P. Gan, B. Yu, B. Guo, J. Chen, M. Wang, J. Zhang, X. Li, J. Zhang and F. Li, *Adv. Funct. Mater.*, 2024, **34**, 2403101.
37 Z. Wang, W. Huang, H. Wu, Y. Wu, K. Shi, J. Li, W. Zhang and Q. Liu, *Adv. Funct. Mater.*, 2024, **34**, 2409303.
38 W. Zhou, M. Chen, D. Zhao, C. Zhu, N. Wang, W. Lei, Y. Guo and L. Li, *Adv. Funct. Mater.*, 2024, **34**, 2402114.
39 Q. He, S. Gu, T. Wu, S. Zhang, X. Ao, J. Yang and Z. Wen, *Chem. Eng. J.*, 2017, **330**, 764–773.
40 A. Pendashteh, J. Palma, M. Anderson and R. Marcilla, *J. Mater. Chem. A*, 2015, **3**, 16849–16859.
41 Z. Zhang, L. Jia, T. Li, J. Qian, X. Liang, D. Xue and D. Gao, *J. Energy Chem.*, 2023, **78**, 447–453.
42 H. Hao, T. Hutter, B. L. Boyce, J. Watt, P. Liu and D. Mitlin, *Chem. Rev.*, 2022, **122**, 8053–8125.
43 A. Kim, S. H. Oh, A. Adhikari, B. R. Sathe, S. Kumar and R. Patel, *J. Mater. Chem. A*, 2023, **11**, 7833–7866.
44 Y. Chen, Q. Li, Z. Chen, W. Zeng, Z. Liu, M. Wang, F. Xia, G. Wang and J. Wu, *Adv. Funct. Mater.*, 2024, **34**, 2411542.
45 Y. Jiang, H. Wang, B. Li, Y. Zhang, C. Xie, J. Zhang, G. Chen and C. Niu, *Carbon*, 2016, **107**, 600–606.
46 M. Jing, M. Zhou, G. Li, Z. Chen, W. Xu, X. Chen and Z. Hou, *ACS Appl. Mater. Interfaces*, 2017, **9**, 9662–9668.
47 S.-H. Chung and A. Manthiram, *Adv. Funct. Mater.*, 2014, **24**, 5299–5306.
48 H. Yao, G. Zheng, P.-C. Hsu, D. Kong, J. J. Cha, W. Li, Z. W. Seh, M. T. McDowell, K. Yan, Z. Liang, V. K. Narasimhan and Y. Cui, *Nat. Commun.*, 2014, **5**, 3943.
49 Y. Sharma, N. Sharma, G. V. Subba Rao and B. V. R. Chowdari, *Solid State Ionics*, 2008, **179**, 587–597.
50 T. Yamashita and P. Hayes, *Appl. Surf. Sci.*, 2008, **254**, 2441–2449.
51 Z. Ma, L. Ren, S. Xing, Y. Wu and Y. Gao, *J. Phys. Chem. C*, 2015, **119**, 23068–23074.
52 B. J. Tan, K. J. Klabunde and P. M. A. Sherwood, *J. Am. Chem. Soc.*, 1991, **113**, 855–861.
53 W. Yan, Z. Yang, W. Bian and R. Yang, *Carbon*, 2015, **92**, 74–83.

54 J. Cai, Y. Ding, J. Li, L. Hou, S. Zhao and Y. Zhang, *J. Mater. Sci.:Mater. Electron.*, 2022, **33**, 12832–12845.
55 S. G. Mohamed, S. Y. Attia and H. H. Hassan, *Microporous Mesoporous Mater.*, 2017, **251**, 26–33.
56 S. Lalwani, M. Munjal, G. Singh and R. K. Sharma, *Appl. Surf. Sci.*, 2019, **476**, 1025–1034.
57 Z. Wang, P. Hong, S. Peng, T. Zou, Y. Yang, X. Xing, Z. Wang, R. Zhao, Z. Yan and Y. Wang, *Electrochim. Acta*, 2019, **299**, 312–319.
58 F. Y. Fan, W. C. Carter and Y.-M. Chiang, *Adv. Mater.*, 2015, **27**, 5203–5209.
59 J.-L. Yang, S.-X. Zhao, Y.-M. Lu, X.-T. Zeng, W. Lv and G.-Z. Cao, *J. Mater. Chem. A*, 2020, **8**, 231–241.
60 Y. Zhu, S. Xiao, Y. Shi, Y. Yang, Y. Hou and Y. Wu, *Adv. Energy Mater.*, 2014, **4**, 1300647.
61 C. Ma, Y. Feng, X. Liu, Y. Yang, L. Zhou, L. Chen, C. Yan and W. Wei, *Energy Storage Mater.*, 2020, **32**, 46–54.
62 E. Jing, L. Chen, S. Xu, W. Tian, D. Zhang, N. Wang, Z. Bai, X. Zhou, S. Liu, D. Duan and X. Qiu, *J. Energy Chem.*, 2022, **64**, 574–582.
63 Y. Dong, D. Cai, T. Li, S. Yang, X. Zhou, Y. Ge, H. Tang, H. Nie and Z. Yang, *ACS Nano*, 2022, **16**, 6414–6425.